# Role of hygroscopic chloride salts on corrosion performance and hydrogen absorption of steel under cyclic wet-dry conditions

Xiaole Han [a] and Masatoshi Sakairi [b]

[a] Graduate School of Engineering, Hokkaido University, Kita-13, Nishi-8, Kita-ku, Sapporo 060-8628, Japan. E-mail address: hansyole@eis.hokudai.ac.jp
[b] Faculty of Engineering, Hokkaido University, Kita-13, Nishi-8, Kita-ku, Sapporo 060-8628, Japan. E-mail address: msakairi@eng.hokudai.ac.jp

## Abstract

The corrosion morphology of steel under aqueous NaCl, $MgCl_2$, and $ZnCl_2$ droplets and the corresponding hydrogen permeation behaviour were investigated using surface characterization techniques and electrochemical methods. Under cyclic wet-dry conditions, $Mg^{2+}$ and $Zn^{2+}$-containing surface layers were formed on steel and the latter presented a high corrosion resistance. The most active hydrogen entry occurred under $ZnCl_2$ during drying, while it happened under $MgCl_2$ at low humidity. The effects of chloride salts on the formation of rust layers and hydrogen entry into steel during wet-dry cycles were discussed based on the hardness of metal cations and the deliquescence properties of salts.

## Keywords

Steel; Hydrogen permeation; SEM; XPS; Atmospheric corrosion; Hydrogen absorption

## 1. Introduction

Atmospheric corrosion is a ubiquitous environmental degradation of steel in service. With the development and wide applications of high-strength steels, the hydrogen produced concomitantly during atmospheric corrosion presents a cracking risk to the durability of steel components due to the embrittling effect of hydrogen after entering the steel [1-4]. Since hygroscopic salts in atmospheric aerosols can introduce conductive electrolytes to the steel surfaces and accelerate the corrosion reactions [5-7], it is essential to elucidate the mechanism of hydrogen entry into steel under salt-induced atmospheric corrosion to reduce the risk of damage to steel structures.

The hygroscopic nature of the deposited salts is a primary concern in atmospheric corrosion. Evans [8,9] has made vital contributions to the scientific understanding of the atmospheric corrosion mechanism of metals under salt deposits and proposed the importance of hygroscopic salts and corrosion products for the occurrence of electrochemical corrosion. It is known that daily changes in air temperature and relative humidity (RH) over time are prominent features of atmospheric environments. Once RH rises above the deliquescence RH (DRH) of a specific salt, the salt and atmospheric moisture combine to form an electrolyte droplet on the substrate. Conversely, as RH falls below the efflorescence RH (ERH), the droplet evaporates until the salt crystallizes with the release of all remaining water [10]. Consequently, with the variation of RH in the atmospheric environments, the deposited salts are responsible for the thickness of the electrolyte films on steel and determine the duration of the corrosion processes, usually defined as the time of wetness (TOW) [11,12].

In coastal areas, atmospheric aerosols frequently contain significant proportions of hygroscopic salts such as NaCl and $MgCl_2$ [6]. As corrosion proceeds under the salt deposits, new hygroscopic salts such as $ZnCl_2$ and $AlCl_3$ may emerge due to the anodic dissolution of Zn-Al containing protective coatings on steel [13-16]. Table 1 summarizes the hygroscopic properties of the salts that are supposed to be present in atmospheric corrosion. It has been reported that the salts with lower DRH values facilitate the corrosion activities and hydrogen absorption processes during atmospheric corrosion [20-22]. Given the experimental findings, a reasonable hypothesis is that the concept of TOW is also practicable to understand the association between hygroscopic salts and the hydrogen absorption behaviour in the corrosion

processes. Unfortunately, there has been limited literature to provide more experimental evidence for this hypothesis.

During the corrosion processes of steel under salt deposits, metal cations in the electrolytes are another important consideration for investigating the hydrogen absorption behaviour. Accompanying the anodic metal dissolution, a proportion of dissolved metal cations can hydrolyse and cause localized acidification [23], which is increasingly considered a prominent source of absorbed hydrogen into metals [24-27]. Regarding the metal cations dissolved from the deposited salts, it has been reported that $Al^{3+}$ accelerates hydrogen absorption into steel during cyclic corrosion compared with $Na^{+}$ [21]. Moreover, $Mg^{2+}$ and $Zn^{2+}$ have been found to participate during the corrosion processes and affect the corrosion kinetics [28,29]. The considerable influences of these cations on the corrosion processes make it critical to investigate their role in hydrogen entry into steel during atmospheric corrosion.

As metal cations can be quantitatively classified according to their acid strengths, the Hard and Soft Acids and Bases (HSAB) concept [30] has been introduced to explain the effects of metal cations on corrosion kinetics [31-34]. Misono et al. [35,36] proposed a dual parameter equation for metal ions to predict the stability of metal-ion complexes as follows:

$$\log K = \alpha X + \beta Y + \gamma \quad (1)$$

where K is the stability constant, X and Y are the dual parameters for the acids and are related to hardness and softness, respectively, α and β are the parameters for the bases, and γ is a constant determined for each base. The parameter X is regarded as cation hardness and is derived from Eq. (2):

$$X = {x_i}^2/10 \quad (2)$$

where $x_i$ is the electronegativity of the metal cation. Table 1 lists the parameter X of each metal cation of interest from the literature [35]. Based on Eq. (1), some researchers reported that the corrosion rate was inhibited with the increase of parameter X of the metal cations in the electrolytes [34,37]. A reasonable mechanism is that a harder metal cation has a stronger affinity to be incorporated into the passive film that contains extensive hydroxide and bond water [31,32,38], and their corporation protects the metal from chloride ions [34]. However, their work was performed in bulk electrolyte environments, and the applicability of the HSAB concept in cyclic wet-dry environments remains to be demonstrated.

The present work aims to investigate the role of hygroscopic salts in corrosion and hydrogen entry into steel under simulated atmospheric conditions and to examine the applicability of the TOW and HSAB concepts in explaining the role of salts in corrosion and hydrogen absorption activity under salt deposits. As listed in Table 1, the distinct difference between the DRH values of the salts is favourable to examining the association between the deliquescence nature of the salts and hydrogen uptake during cyclic wet-dry corrosion. Furthermore, the difference in parameter X corresponding to the cation hardness of the salts provides a feasible way to compare the effect of the metal cations on corrosion and hydrogen entry into steel.

## 2. Experimental

### 2.1 Samples and salt solutions

The material tested was Cr-Mo steel with a Japanese Industrial Standard (JIS) grade of SCM435 (C: 0.35, Si: 0.18, Mn: 0.74, P: 0.0011, S: 0.0017, Cr: 1.15, Mo: 0.15, Fe: balance, all in mass%) and was machined into samples with dimensions of 20 mm × 15 mm × 1 mm. The samples were subsequently embedded in cold-curing resin and mechanically ground with SiC grinding papers up to 2400 grit. The polished surfaces (20 mm × 15 mm) were cleaned sequentially with ethanol and highly purified water in an ultrasonic bath for 300 s. In order to avoid the instability of current changes due to the passivation of sample surfaces during the anodic polarization in the following hydrogen permeation test, one side of the samples was electroplated with a Ni layer of approximately 1 μm thick using a 0.312 M $NiSO_4$/0.781 M $H_3BO_3$ solution at a current density of 4 mA $cm^{-2}$ for 720 s. The Ni plating exhibited good reproducibility and was effective for the detection of permeated hydrogen through the samples.

The chloride salts of interest in the present work were NaCl, $MgCl_2$, and $ZnCl_2$. To simulate the corrosion of steel by these chlorides incorporated with airborne droplets, salt solution droplets with volumes of 10 μL were deposited onto the samples and the droplet contact diameters were about 5 mm. NaCl is the most common and abundant airborne salt, and its concentration used in this work was 10 mM to make the amount of deposited chloride close to the actual environments at weathering sites across Japan [2]. Since $Cl^-$ is a well-known aggressive anion and has a significant influence on corrosion performance, the concentration

of $Cl^-$ in each salt droplet was controlled at 10 mM in order to compare the effects of metal cations on corrosion. The salt solutions were prepared using analytic grade reagents (Kanto Chemical Co., Inc., Japan) and ultrapure water at room temperature, as listed in Table 2. Two groups of mixed salt solutions were prepared using aqueous NaCl and other salt solutions.

2.2 Hydrogen permeation test

An electrochemical apparatus (Fig. 1(a)) based on the Devanathan-Stachurski cell [39] was employed to record the permeation current of hydrogen that was produced on one corroding side and then diffused through the sample. The apparatus consisted of a hydrogen detection cell and an upper exposed area where the corrosion occurred, which were separated by the sample. The Ni-plated surface of the sample was in contact with the hydrogen detection cell and acted as the working electrode (WE). The counter electrode (CE) and reference electrode (RE) were made of Pt wires of 0.5 mm in diameter and were fixed in the detection cell filled with 1 M NaOH solution. The opposite surface of the sample was prepared for the placement of droplets that would initiate the corrosion. The sample was then bolted between two rubber rings so that both sides had the same exposed area of 28.27 $mm^2$. The absence of gas bubbles in the detection cell was confirmed before the subsequent polarization procedures.

The assembled electrochemical cell was installed horizontally in a temperature and humidity chamber (IW243, Yamato Scientific Co., Ltd., Japan) as presented in Fig.1(b). Prior to the corrosion test, the sample was pre-polarized at a constant anodic potential of -30 mV vs. Pt using a highly sensitive potentiostat (HECS 318C, Fuso, Kawasaki, Japan) until the background current reached a steady value and fell below 20 nA $cm^{-2}$, which required about 24 h. The anodic potential of -30 mV vs. Pt was sufficient to ensure rapid ionization of the permeated hydrogen atoms from the sample and was employed in all hydrogen permeation tests in the study. The salt solution with a volume of 10 μL was placed as a droplet on the surface of the sample using a microliter pipette. Simultaneously, the changes in the anodic current attributed to the ionization of diffused hydrogen atoms from the corrosion side were recorded.

Considering the time delay from the generation of absorbed hydrogen to the diffusion through samples and finally being detected, an accelerated corrosion test was conducted on the samples to measure the required response time of hydrogen permeation and the details of the

procedure have been reported elsewhere [40]. Finally, a time delay of about 13 min was used in discussing the relationship between the change in corrosion morphology and hydrogen permeation currents.

### 2.3 Cyclic corrosion test

The temperature and humidity chamber (Fig. 1(b)) was used to simulate a cyclic wet-dry environment. After the placement of the aqueous salt solutions in the form of droplets on the sample, the temperature and humidity inside the chamber were controlled according to a pre-designed procedure. A typical cycle of the wet-dry condition was plotted in Fig. 1(c). Considering the DRH and ERH values of the salts, the RH variation was set from 90% to 20% to achieve the wet-dry conditions. The design of the variation of temperature was intended to keep the environment at a constant dew point of 25 ˚C. However, the temperature interval in the experiments was narrowed to 30 ˚C to 50 ˚C to avoid current noise caused by excessive temperature changes in the hydrogen detection cell. The changes in temperature and humidity in one cycle (6 h) consist of four stages: wet (1 h), drying (1 h), dry (3 h), and wetting (1 h) to the initial wet condition. Each group of corrosion tests was carried out for 12 consecutive cycles (72 h). A thermos-hygrometer was fixed above the sample to ensure that the desired temperature and humidity were achieved throughout the whole experiment. The airflow inside the chamber functioning for air circulation was another essential parameter in the corrosion process, with a velocity of 1.4 m/s above the samples. The cyclic corrosion tests combined with hydrogen detection were carried out at least three times for each salt solution to ascertain the reproducibility of appreciable phenomena during the experiments.

### 2.4 Surface characterisation and analysis

An autofocus USB camera (Reson Lighting Technology Co., Ltd., China) with 1080 p resolution was used for surface imaging during the corrosion process of the sample. The surface changes were captured at intervals of 30 s for the initial three cycles (18 h) of the cyclic corrosion test. After the corrosion tests, micrographs of the corroded surface were taken using an optical microscope (OM, MV-550, WRAYMER Inc., Japan). ImageJ [41] was used to calculate the area statistics of the corroded surfaces of the samples. For characterisation under

the rust layer, the corrosion products on the samples were removed carefully using a polishing machine, and then the surfaces were observed using OM.

The surface characterisation and corrosion product analysis were performed with a scanning electron microscope (SEM, JSM-6510-LA, JEOL Ltd., Japan) equipped with an energy dispersive X-ray spectrometer (EDS). The accelerating voltage of the incident electron beam was set at 10 kV for the SEM observation and 20 kV for the EDS analysis. The cross-section of the corroded surface was obtained using a cross-section polisher (IB-19520CCP, JEOL Ltd., Japan) and investigated using SEM and EDS.

An X-ray photoelectron spectroscope (XPS, JPS-9200, JEOL Ltd., Japan) with an Mg Kα X-ray source was used to identify the elements and their chemical states in the sample surfaces. The samples used for XPS analysis were ultrasonically cleaned in purified water for 300 s to remove the residual corrosion products on the surfaces. The analysis area was a 3 mm diameter region centred on the corrosion zone. The curve fitting procedures were conducted in CasaXPS software and the adventitious carbon peak at 284.8 eV was used for charge correction. An auger electron spectrometer (AES, JAMP-9500F, JEOL Ltd., Japan) with a spatial surface resolution of the order of 6 nm was used to characterize the corrosion products. The samples were cut into suitable dimensions using a cut-off machine with water cooling due to the size limitation of the samples for the AES analysis. AES spectra of selected points on the samples were obtained with an accelerating voltage of 10 kV and a probe diameter of the order of 10 nm.

## 3. Results

### 3.1 Corrosion and hydrogen absorption of steel in the first wet-dry cycle

To investigate the role of metal cations, $Na^+$, $Mg^{2+}$, and $Zn^{2+}$, in the corrosion and hydrogen absorption processes of steel under different salt droplets, this study observed the corrosion morphology and the corresponding hydrogen permeation currents of steel samples under the NaCl, $MgCl_2$, and $ZnCl_2$ droplets.

#### 3.1.1 Changes in corrosion morphology of steel under salt droplets

Fig. 2 presents a series of optical images showing the surface changes of the samples during the initial wet-dry stage, which are selected from a time-lapse video (see supplementary

material) that records the surface changes of the samples during the initial three cycles. The deposited droplets have approximately the same size and shape at the beginning of the corrosion tests. After the start of the wet-dry cycle, corrosion occurs rapidly on the samples under the droplets containing $Na^+$ and $Mg^{2+}$. Yellow flocculent corrosion products appear on the surfaces after 10 min (Movie S1) and relatively black regions can be observed near the central areas of the samples (Fig. 2(a) and (b), indicated by white arrows). These black areas indicate the initiation of anodic dissolution of iron. After one hour, the area covered by yellow corrosion products under the NaCl droplet is greater than that under $MgCl_2$, and the products tend to precipitate in the region between the centre and edge of the droplets. In the case of the $Zn^{2+}$-containing droplet, no visible corrosion products can be observed in the first hour until the appearance of a black spot (Fig. 2(c), white arrow) in the central area, surrounded by a slight white layer. These observations demonstrate that the corrosion process is most active under the NaCl and $MgCl_2$ droplets and is greatly inhibited when the droplet contains $Zn^{2+}$.

As the RH decreases from 90% to 20% and droplets begin to evaporate in the drying period, the amount of rust on the samples under NaCl and $MgCl_2$ droplets increases, and ring-shaped rust layers can be found along the peripheral regions of the droplets (Fig. 2(a) and (b), black arrows), leaving white layers at the outermost peripheries. About halfway through the drying period, a distinct transition of the surfaces from visible wet to dry appears on all the samples (Fig. 2 and Movie S1). The white layers formed under NaCl extend almost to the edge of the exposed surface, whereas those under $MgCl_2$ are along the initial droplet rim. Remarkably, the surface morphology of the sample under $ZnCl_2$ presents a particular phenomenon. As shown in Fig. 2(c) and Movie S1, a yellow rust layer gradually forms around the initial black spot instead of large amounts of flocculent corrosion products. In addition, the yellow layer prefers to form towards one side of the peripheral region, leaving a visible uncorroded area covered by a white film. This phenomenon is related to the influence of airflow inside the chamber. According to the wind direction as shown in Fig. 2 and Movie S1, the windward side of the sample surfaces becomes dry more quickly than the leeward side. The faster airflow and higher oxygen content on the windward side may be the reason for the formation of white films. The composition of these surface films will be investigated in the following section.

In the dry period, the RH is steady at 20% which is lower than the ERH of NaCl but higher

than that of $MgCl_2$ and $ZnCl_2$. In the case of the sample under the $MgCl_2$ deposition, it is apparent that new corrosion products are present on the previous white layers along peripheral regions of the rust ring (Fig. 2(b) and Movie S1). Additionally, the previous black corrosion products turn brown in the dry period (Fig. 2(b), yellow arrows). As demonstrated in the literature [9], the colour change of the corrosion products is probably related to the oxidation of black magnetite to brown rust by oxygen. By contrast, no perceptible development of the corrosion products under the other salt depositions can be observed from optical observations. These phenomena suggest that the $MgCl_2$ deposition allows for the corrosion process to continue even under low humidity, while the $ZnCl_2$ deposition, which can absorb moisture more easily than $MgCl_2$, has no promotion effect on corrosion.

When the RH increases from 20% to 90%, appreciable amounts of new black corrosion products appear on the rust layers during the second half of the wetting period (Fig. 2 and Movie S1). According to the well-accepted mechanism of atmospheric rusting of iron [9], the conversion of brown rust layers to black magnetite takes place accompanied by the anodic dissolution of iron in the presence of water. Therefore, the colour change indicates active corrosion processes when the surfaces become wet again.

### 3.1.2 Hydrogen permeation during the corrosion of steel under salt droplets

Fig. 3(a) shows the records of the hydrogen permeation current densities corresponding to the initial wet-dry cycle of the corrosion processes (Fig. 2). The current variation represents the instantaneous rate of hydrogen permeation through the samples. In the first wet period, the currents remain nearly unchanged before the droplets begin to evaporate. This suggests that no appreciable hydrogen permeation occurs under the droplets, although an appreciable amount of corrosion products is formed on the samples under the NaCl and $MgCl_2$ droplets (Fig. 2(a) and (b)). Afterwards, the currents show a pronounced increase in the drying period, indicating the production of a significant amount of diffused hydrogen with increasing temperature and decreasing RH. It is noteworthy that the current of the sample under the $ZnCl_2$ droplet initiates a prompt increase after a noticeable delay compared with the other two conditions. The delayed current increase indicates the inhibition of $Zn^{2+}$ on the hydrogen absorption activity before droplet drying. On the other hand, the current under $ZnCl_2$ shows the most significant increase

than other salts, suggesting the acceleration effect of $ZnCl_2$ on hydrogen absorption during the drying period.

After the beginning of the dry stage, the currents begin to decline after reaching a maximum value. The appearance of the decay transient indicates the retardation or stagnation of the hydrogen entry into samples. Significantly, the current of the sample exposed to the $MgCl_2$ deposition exhibits a diminished decline and remains at high values at the end of the dry period. This particular phenomenon reveals that although the corrosion reaction is supposed to be hindered due to the lack of electrolytes under dry conditions, the hydrogen absorption reactions remain active at the entry surface. Corresponding to the corrosion morphology in the dry period shown in Fig. 2(b), the proceeding of the corrosion processes under the $MgCl_2$ deposition is responsible for providing the hydrogen source.

In the final wetting period, the current curves present an initial quick decline due to the decrease in temperature. Subsequently, the curves exhibit a camel-shaped change with increasing RH. According to the surface observations in Movie S1, the current rises occur earlier than the appearance of large amounts of black corrosion products. This phenomenon indicates that a higher RH contributes to the corrosion process without accelerating hydrogen entry into steel. As the deposited salts absorb moisture with increasing RH, the acceleration of hydrogen absorption is considered to be attributed to the initial thin electrolyte layers rather than a larger volume of electrolytes. A higher concentration of corrosive ions within the rust layers may be necessary for hydrogen evolution and absorption reactions.

Fig. 3(b) shows the hydrogen contents by integrating the current densities of the samples under salt droplets during each period of the first wet-dry cycle. Combined with the changes in permeation currents in Fig. 3(a), the quantitative analysis of the diffused hydrogen suggests that the initial drying to wetting periods predominate in the hydrogen entry into steel during the corrosion process under salt droplets. In other words, thin electrolyte layers with high concentrations of aggressive ions play a dominant role in the hydrogen absorption reactions. Moreover, the quantity of diffused hydrogen through the samples under $MgCl_2$ and $ZnCl_2$ droplets is significantly larger than that under NaCl droplets, which suggests that the lower ERH and DRH values of salts extend the presence of electrolyte layer and contribute to the hydrogen uptake by samples. However, although $ZnCl_2$ has the strongest ability to absorb

moisture and maintain the presence of electrolyte layers, the quantity of absorbed hydrogen under the $ZnCl_2$ deposition is lower than that under $MgCl_2$, which might be attributed to the inhibition effect of $Zn^{2+}$ on the corrosion process of steel.

### 3.2 Formation of $Mg^{2+}$/ $Zn^{2+}$-containing films on steel under salt droplets

During each stage of the first wet-dry cycle, the composition of salt droplets presents a significant effect on the corrosion morphology and the corresponding hydrogen absorption activity. To investigate the role of $Na^+$, $Mg^{2+}$, and $Zn^{2+}$ in the rust formation during the drying of salt droplets, XPS analysis was performed on the sample surfaces during the initial wet-dry cycle. After the samples were corroded under salt droplets for 1 h, Mg 1s, auger Mg KLL, Zn $2p_{2/3}$, and auger Zn LMM peaks were detected in the wide-scan XPS spectra as shown in Fig. 4(a). Since the samples were ultrasonically cleaned before XPS analysis, the results demonstrate that the metal cations, $Mg^{2+}$ and $Zn^{2+}$, were incorporated into the surface films of steel during the corrosion process under salt droplets. Regarding the composition of corrosion products, the narrow-scan XPS spectra of O 1s indicate that the surface layers are mainly composed of hydroxide and oxide (Fig. S1). Although the C 1s spectra suggest the presence of carbonates, the contribution of the C-O and O-C=O bonds to the O 1s spectra is smaller than the oxide and hydroxide bonds. The XPS spectra of Mg 1s and Zn $2p_{2/3}$ shown in Fig. 4(b) exhibit the chemical states of the metal cations on the sample surfaces. The binding energy of the Mg 1s peak can be fitted into two peaks centred at 1304.03 eV and 1303.27 eV, which are related to the binding energies of MgO and $Mg(OH)_2$, respectively [42]. The peak of Zn $2p_{2/3}$ is centred at 1021.47 eV and agrees with the binding energy of ZnO [43].

In the following drying period, water evaporation accelerates the formation of corrosion products at the sample surfaces. After the drying procedure, the samples were ultrasonically cleaned again in purified water before XPS analysis. As shown in Fig. 4(a), Mg was not detected in the wide-scan XPS spectra after droplet drying (2 h). The MgO and $Mg(OH)_2$ films formed previously under $MgCl_2$ droplets are supposed to be destroyed by accelerated corrosion as water evaporates. On the other hand, the narrow-scan spectrum of Zn $2p_{2/3}$ presenting a peak of 1021.48 eV demonstrates the presence of Zn in the form of ZnO after droplet drying. The results suggest that metal cations such as $Mg^{2+}$ and $Zn^{2+}$ contribute to the formation of oxide and

hydroxide films on steel surfaces under salt droplets. Furthermore, the formation of ZnO significantly enhances the stability of the steel surfaces and makes the steel less susceptible to corrosion attack.

### 3.3 Corrosion morphology and hydrogen absorption of steel after droplet drying

In the subsequent wet-dry cycles, as no external supplement of water to the sample surfaces, the hygroscopic nature of the deposited salts was responsible for the formation of electrolytes with the variation of RH and temperature. Fig. 5 and Movie S1 show the corrosion morphology of the samples during the second and third wet-dry cycles. After the droplets evaporate, the changes in the sample surfaces are not distinct in the following wet-dry cycles. However, some new corrosion products can be observed near the existing rust layers after three cycles, as indicated in the white dotted circles. Additionally, an obvious accumulation of dark corrosion products can be observed on the peripheries of the corroded surface, forming rust rings as indicated in the yellow dotted circles. In the case of the sample under $ZnCl_2$ deposition, the density of dark corrosion products is densely concentrated on one side of the corroded surface, and new corrosion products are also formed on the light corrosion layers. This result indicates the gradual breakdown of the $Zn^{2+}$-containing films during wet-dry cycles.

Fig. 6(a) shows the changes in hydrogen permeation current densities during the following corrosion processes. Although the current curves exhibit prominent differences in the amplitude of the current density, their variations in each cycle present a similar tendency involving four distinct stages. The permeation currents start from relatively low values in the initial wet period, keeping steady or increasing gradually, then exhibit a conspicuous increase in the drying period, and finally decrease in the subsequent dry and wetting periods. This variation tendency in each cycle reveals that the hydrogen uptake occurs at a slow rate when the RH is high to maintain the surface being wet, while the drying stage accelerates hydrogen uptake into steel. Regarding the differences in the permeation currents under different exposure conditions, there are three features worth describing. First, the permeation curves under $ZnCl_2$ deposition exhibit larger maximum values than other conditions in most cases, indicating that the hydrogen uptake is promoted by the deposition of $ZnCl_2$. Second, the current under $MgCl_2$ deposition shows a slow decline at the dry stage, suggesting that hydrogen uptake is still active even though the RH is

low. The third is that all permeation curves tend to be similar with increasing cycle number and no distinct difference appears in all permeation curves after the tenth cycle.

Fig. 6(b) shows the hydrogen contents of the samples under salt deposits in the last eleven cycles. Accompanied by the cyclic corrosion of samples, a considerable amount of permeated hydrogen can be observed in each stage of one wet-dry cycle. The drying and dry stages are the predominant periods for the hydrogen entry into steel. In addition, the hydrogen uptake under $MgCl_2$ and $ZnCl_2$ depositions is more active than that under NaCl deposition. It is worthwhile to note that the electric charge under $ZnCl_2$ deposition has a large deviation during the wet-dry cycle. The large difference in the amount of permeated hydrogen during corrosion under $ZnCl_2$ will be discussed later.

### 3.4 Characterization of corroded surfaces using SEM-EDS and AES

To investigate the effect of salts on the corrosion morphology of samples after 12 wet-dry cycles, SEM observation and EDS analysis were performed on the corroded surfaces. Fig. 7(a) shows a corroded area near the rust ring of the sample under NaCl. Some raised spherical corrosion products can be observed adjacent to the rust ring, while the relatively uniform ones are homogeneously distributed in the flat region near the central area of the exposed surface. The EDS elemental mapping shows that Cl is particularly abundant in the raised structures of the corrosion products, and the detection of Na and Cl in the same area (Fig. 7(a), white arrows) indicates the accumulation of NaCl around the rust ring after 12 cycles of corrosion. In Fig. 7(b), the SEM observations on the sample exposed to $MgCl_2$ show that the surface is covered by raised corrosion products and a portion of the surface is not significantly corroded, as indicated in the white arrow. Moreover, the EDS analysis illustrates the presence of a great proportion of Mg-containing precipitation layers adjacent to the raised corrosion products.

The corrosion products formed on the sample exposed to $ZnCl_2$ exhibit a distinct boundary between the flat (Area 1) and raised (Area 2) regions. EDS analysis performed on a selected boundary area shows that the raised area contains large amounts of corrosion products and Cl is significantly abundant in the raised spherical corrosion products similar to the other two salts. In particular, Zn exhibits no particular aggregation on the corroded surface and only a rare proportion is detected on the flat area. To further determine the presence of Zn on the surface,

AES analysis was carried out on the flat region (Fig. 8(a), Area 1) and raised region (Fig. 8(a), Area 2) and the results are presented in Fig. 8(b). The Zn is primarily found in the uniform rust layer but not in the raised corrosion products. The detailed auger spectra of Zn (Fig. 8(c)) illustrate that Zn is probably in the form of its oxide and hydroxide as the kinetic energy of Zn peaks shows a slight shift in the energy reduction direction compared with the standard spectrum.

### 3.5 Analysis of corroded surfaces under rust layers

#### 3.5.1 Section analysis of samples after cyclic wet-dry corrosion

The cross-sectional images of the corroded surfaces provide additional information on the morphology of the corrosion products. The rust layers formed on the sample under NaCl are porous and contain cracks, as shown in Fig. 9(a). Abundant porous structures can be observed in the inner rust layer near the steel substrate. Furthermore, the interface between the rust layer and the steel substrate is relatively flat compared with other salts, as indicated by the dashed lines. In the case of the sample under $MgCl_2$ (Fig. 9(b)), the thickness of the rust layers is significantly greater than the sample under NaCl. In addition, deep and elliptical corrosion pits are formed under hill-shaped corrosion products. Similarly, the rust layer under $MgCl_2$ also contained cracks but in near horizontal shapes, and the porous structures are remarkably abundant in the hill-shaped layers. As for the sample under $ZnCl_2$, Fig. 9(c) shows two distinct areas under flat and raised corrosion products, corresponding to Area 1 and Area 2 in Fig. 7(c), respectively. The flat area, where Zn has been determined to be present, has a relatively thin rust layer and suffers from a slight pitting corrosion. The area under a large amount of raised corrosion products presents a similar feature to that under $MgCl_2$, consisting of pits and porous rust layers. Although it is rare to find the elements of Na, Mg, and Zn in the rust layers from the EDS elemental mapping on the cross-sectional samples (Fig. S2), the element Cl is particularly abundant near the surface of the hill-shaped corrosion products. The distinct boundary between the rust layer and steel substrate also indicates the presence of larger pits under $MgCl_2$ and $ZnCl_2$ deposits than NaCl. As mentioned previously, lower ERH and DRH values of the $MgCl_2$ and $ZnCl_2$ deposits can provide a prolonged period for corrosion proceeding and hydrogen entry into steel. Coupled with the results of cross-sectional images, the greater number of pits under

$MgCl_2$ and $ZnCl_2$ deposits than NaCl is probably attributed to the higher deliquescent properties of the salts. Accordingly, it is reasonable to assume that the promotion effect of hygroscopic salts on the pitting development under rust layers may be responsible for the higher hydrogen permeation charge during wet-dry corrosion.

3.5.2 Area calculation of corroded surfaces under rust layers

To corroborate the finding of the acceleration effect of pitting corrosion on the hydrogen entry into steel, this study attempted to calculate the pitting area of the corroded samples under different salt depositions. As shown in Fig. 10, each sample after corrosion under different deposited salts has distinctive characteristics of corrosion products. The corroded surfaces of each sample mainly consist of a ring-shaped brown layer along the peripheral region and other orange corrosion products. Significantly, the brown ones correspond to the hill-shaped rust layers where appreciable pits can be found, as shown in Fig. 9. The orange ones, by contrast, are related to the flat rust layers where general corrosion predominately occurs. From the images after removing the rust layer using the polishing machine, the pitted areas are prominently distributed under the brown hill-shaped corrosion products, leaving the relatively uncorroded steel substrate under the orange ones. This finding corroborates the connection between the pitting region and the brown rust area. The area beneath the brown rust ring is one of the prime places for pitting corrosion. In particular, the sample under $ZnCl_2$ shows a serious pitted region under a brown spot near the central area (Fig. 10(c), red arrow), corresponding to the previous black spot that appeared in the wet period of the first cycle (Fig. 2(c), white arrows). This result confirms the corrosion mechanism that initial anodic dissolution usually happens near the central area of the salt droplets.

For the sake of simplicity, the brown and orange corrosion products were categorised as pitting and intact regions, respectively. Based on the colour difference in the corroded products, region selection was carried out in ImageJ software. Since the brown colour represents the pitting area, the red-green-blue (RGB) codes from (0, 0, 0) to (255, 120-140, 255) were derived from the optical images (Fig. 10). The ratio of the pitting area to the entire exposed area was calculated and plotted against the amount of diffused hydrogen under five kinds of salt depositions. As shown in Fig. 11, the greater amount of permeated hydrogen is related to the

greater percentage of the pitting area. The large difference in the pitting area under the same composition of salt droplets results in a large deviation in the amount of permeated hydrogen, as mentioned in Fig. 6(b). Moreover, the results show that the amount of permeated hydrogen of the samples under $MgCl_2$-containing salts is greater than that under $ZnCl_2$, although the samples have a similar percentage of pitting area. Based on the cross-sectional images of the pitting area under $MgCl_2$ and $ZnCl_2$, the deeper pits under $MgCl_2$ are supposed to be responsible for the more active entry of hydrogen into the steel.

## 4. Discussion

According to the corrosion performance and hydrogen absorption behaviour of steel under cyclic wet-dry conditions, this study suggests that the salts play a different role in two stages, before the drying of droplets and after the formation of rust layers with water evaporation.

### 4.1 Role of salts in corrosion and hydrogen absorption under droplets

When the corrosion takes place under salt droplets, the composition of the electrolytes has a distinct influence on the corrosion morphology, and no perceptible hydrogen entry occurs at this stage. To explain the corrosion process of steels under droplets, a well-known droplet model proposed by Evans provides insight into the effect of the oxygen concentration gradient in the droplet [44]. The corrosion morphology observed in the present study generally follows this mechanism. The droplet shape facilitates the access of oxygen to the steel surface through the edge of the droplet and thus establishes a concentration cell with the edge area acting as the cathode and the central area acting as the anode. Ferrous ions released from the anode migrate to the peripheral area and combine with hydroxide ions produced by the oxygen reduction reaction (ORR) to form rust. Therefore, the results of this study indicate that when corrosion occurs under salt droplets, the predominant reactions are anodic iron dissolution and cathodic ORR.

In this study, the metal cations of the salts present a different ability to form barrier layers to corrosion attack under droplets. As corrosion proceeds under salt droplets, $Mg^{2+}$ and $Zn^{2+}$ can introduce hydroxide/oxide components into the steel surfaces. In particular, the $Zn^{2+}$-

containing films have a better corrosion resistance than $Mg^{2+}$-containing films and cannot be destroyed easily with corrosion proceeding. Compared with previous work [21], the corrosion morphology of steel under $AlCl_3$ droplet is similar to that under $ZnCl_2$, and the precipitated layers containing $Al_2O_3$ present an ability to retard iron dissolution before the droplet evaporates. Given that the hardness of metal cations decreases from $Al^{3+}$ to $Na^+$ as listed in Table 1, it is reasonable to assume that the metal cations with higher hardness contribute to the formation of protective films with higher corrosion resistance. The surface observations and XPS analysis demonstrate that the cation-combined protective films form at an early stage (less than 10 min after the deposition of salt droplets) before the formation of corrosion products. Accordingly, the improvement of corrosion resistance of surface layers is probably attributed to the formation of hydroxide/oxide films of harder metal cations such as $Zn^{2+}$ on the top of the original passive films. Another reasonable mechanism is that the harder metal cations can bind to the passive films and repair the defects to improve corrosion resistance.

Based on a passive film model proposed by Okamoto et al. [38,45], the initial passive film on steel is supposed to be a hydrated oxide film under aqueous salt solutions, containing $H_2O$-Fe-$OH_2$, -HO-Fe-OH-, and -O-Fe-O- structures. As illustrated in Fig. 12(a), when the corrosion of steel takes place under an aqueous NaCl droplet, the chloride ions lead to the localized breakdown or migrate to defective sites of the passive films, accelerating the localized corrosion of the underlying steel. According to the HSAB concept, metal cations with higher hardness acting as hard acids prefer to bind to hard bases such as $H_2O$ and $OH^-$. For this reason, harder metal cations such as $Zn^{2+}$ and $Al^{3+}$ are easier to combine with the hard bases of the passive film of steel. As illustrated in Fig. 12(b), $Zn^{2+}$ in the electrolytes binds to the hydrated oxide on the top of the passive film or repairs the defective sites of the passive film, inhibiting the corrosion attack from chloride ions. In addition, the combination of metal cations and the passive films accelerates the deprotonation of the passive film and contributes to the formation of well-developed oxide films (-O-M-O-) [45]. As a result, harder metal cations such as $Zn^{2+}$ and $Al^{3+}$ introduce the formation of stable oxides such as ZnO and $Al_2O_3$, presenting an inhibition effect on the corrosion of steel under salt droplets.

4.2 Role of salts in corrosion and hydrogen absorption after droplet drying

As water evaporates in the drying stage, the increasing concentration of aggressive anions leads to the breakdown of passive films and results in accelerated corrosion of steel and hydrogen absorption process. It is known that the presence of electrolytes is essential for electrochemical corrosion to proceed, and therefore the deliquescence properties of the salts will play a predominant role after droplet drying. The lower DRH and ERH values of the salts represent the stronger capacity to absorb moisture, providing a longer time for the existence of a thin layer of electrolyte. Further, it is important to consider the high concentration of aggressive anions such as $Cl^-$ in the thin electrolyte layer. As mentioned in Section 3.1.2, hydrogen entry into steel can be accelerated in the presence of a thin electrolyte layer with a high concentration of corrosive ions. Therefore, high hygroscopic salts such as $MgCl_2$ and $ZnCl_2$ afford a prolonged TOW for corrosion and hydrogen absorption reactions to proceed during wet-dry cycles.

On the other hand, the presence of rust layers is another important factor influencing the hygroscopicity of the deposited salts on steel surfaces. As proved in Fig. 9, the rust layers contain narrow cracks and porous structures. Attributing to the capillary condensation of the porous structure, the deposited hygroscopic salts can retain the presence of electrolytes within the porous rust layers under low RH conditions, extending the TOW for corrosion during wet-dry cycles, as illustrated in Fig. 12(c). Furthermore, the remaining electrolytes within the rust layers are supposed to have a high concentration of corrosive ions. This is probably the reason why corrosion and hydrogen entry can take place under $MgCl_2$ deposits even when the corroded surfaces have a dry appearance in the dry stage (Fig. 2(b) and Fig. 3(a)). Although $ZnCl_2$ deposits have lower DRH and ERH values than $MgCl_2$, the presence of ZnO inhibits the formation of porous rust layers, resulting in a lower quantity of absorbed hydrogen after an entire wet-dry cycle. After the breakdown of the protective films due to the increasing concentration of corrosive ions in the drying period (Fig. 12 (d)), porous corrosion products accumulate around the anodic dissolution sites, facilitating the absorption of moisture and accelerating corrosion and hydrogen entry under the rust layers. Overall, both the hygroscopicity of the salts and the porous structure of the rust layers are crucial factors in determining the TOW for corrosion and hydrogen absorption processes during wet-dry cycles.

Regarding the mechanism of hydrogen absorption after droplet drying and rust formation,

pitting corrosion and localized acidification under rust layers are suggested to play a vital role in the wet-dry cycles. After the droplets evaporate, the remaining electrolytes with a high concentration of chloride inside the thick and porous rust layers are favourable for the development of new pits under the rust layers, contributing to decreasing pH inside the pits [46]. Since the rust layers retard the migration of ions between the anodic and cathodic areas, the hydrolysis of the dissolved iron also results in acidification inside the pits [3,23,47]. The hydrogen adsorption reaction takes place according to the Volmer mechanism, i.e., the electrochemical reduction of proton in acid solutions (Eq. 3):

$$H^+ + e^- \rightarrow H_{ad} \quad (3)$$

The adsorbed hydrogen atoms are subsequently absorbed by the steel substrate (Eq. 4):

$$H_{ad} \rightarrow H_{ab} \quad (4)$$

Attributing the decreasing pH inside the pits, the driving force for hydrogen evolution reaction is promoted when corrosion potential is assumed to be constant. As a result, the adsorption and absorption reactions of hydrogen are accelerated under the rust layers.

Together, the hygroscopic salts and porous rust layers introduce thin electrolyte layers with high chloride concentrations to the steel surface and contribute to localized acidification under the rust layers. When the deposited salts, such as $MgCl_2$ and $ZnCl_2$, have a higher ability to absorb moisture, the TOW is prolonged for corrosion and hydrogen entry into steel. However, with the increasing we-dry cycle number, the increasing thickness of stable rust layers is supposed to retard the access of electrolytes and oxygen to the steel surface; therefore, the corrosion and hydrogen absorption processes will decline progressively under cyclic wet-dry conditions.

## 5. Conclusions

The present study examined the corrosion morphology and the associated hydrogen permeation behaviour of steel after the placement of salt solution droplets and several wet-dry cycles. Several conclusions can be drawn as follows:

(1) When corrosion occurs under salt droplets, $Mg^{2+}$ and $Zn^{2+}$-containing surface layers are formed on the steel surfaces and the latter presents a high corrosion resistance. Based on the HSAB concept, the metal cations that have higher cation hardness,

parameter X, are easier to combine with the hard bases such as $H_2O$ and $OH^-$ of the passive films, forming stable protective passive films against corrosion attack under salt droplets.

(2) After water evaporates and steel surfaces become apparently dry, the hygroscopic property of the salts deposited within the porous rust layers plays a dominant role in the corrosion and hydrogen absorption processes. The salts with low deliquescence values retain the presence of thin electrolyte layers with high chloride concentrations within the porous rust structures, affording a prolonged TOW for localized corrosion.

(3) Pitting corrosion and localized acidification under rust layers are responsible for accelerated hydrogen entry into steel. The presence of ZnO film retards the development of pitting corrosion, thereby reducing the amount of absorbed hydrogen during an entire wet-dry cycle.

**Acknowledgements**

This work was supported by JST SPRING [Grant Number JPMJSP2119]. The authors acknowledge the research groups, “Comprehensive Understanding of Hydrogen-Passive Surface on Steels for Prevention of Hydrogen Embrittlement” and “Corrosion-induced Hydrogen Absorption to Steels” of the Iron and Steel Institute of Japan. A part of this work was conducted at the Laboratory of XPS analysis, Joint-use facilities, Hokkaido University, supported by “Advanced Research Infrastructure for Materials and Nanotechnology in Japan (ARIM)” of the Ministry of Education, Culture, Sports, Science and Technology (MEXT). Proposal Number JPMXP1223HK0028.

## Appendix A. Supplementary material

Supplementary data include one video and two figures.

## CRediT authorship contribution statement

**Xiaole Han**: Conceptualization, Methodology, Validation, Investigation, Data curation, Writing-original draft, Visualization, Funding acquisition.

**Masatoshi Sakairi**: Conceptualization, Methodology, Resources, Writing-review & editing, Supervision, Funding acquisition.

## Data availability

Data will be made available on request.

**References**


[1] M. Nagumo, Function of hydrogen in embrittlement of high-strength steels, ISIJ Int. 41 (2001) 590-598. https://doi.org/10.2355/isijinternational.41.590

[2] T. Kushida, Hydrogen entry into steel by atmospheric corrosion, ISIJ Int. 43 (2003) 470-474. https://doi.org/10.2355/isijinternational.43.470

[3] T. Tsuru, Y. Huang, M.R. Ali, A. Nishikata, Hydrogen entry into steel during atmospheric corrosion process. Corros. Sci. 47 (2005) 2431-2440. https://doi.org/10.1016/j.corsci.2004.10.006

[4] O. Barrera, D. Bombac, Y. Chen, T.D. Daff, E. Galindo-Nava, P. Gong, D. Haley, R. Horton, I. Katzarov, J.R. Kermode, C. Liverani, Understanding and mitigating hydrogen embrittlement of steels: a review of experimental, modelling and design progress from atomistic to continuum, J. Mater. Sci. 53 (2018) 6251-6290. https://doi.org/10.1007/s10853-017-1978-5.

[5] P.R. Roberge, Atmospheric Corrosion, in: R.W. Revie (Ed.), Uhlig's Corrosion Handbook, third ed., Wiley, New York, 2011, pp. 299-326. https://doi.org/10.1002/9780470872864.ch23

[6] C.R. Bryan, A.W. Knight, R.M. Katona, A.C. Sanchez, E.J. Schindelholz, R.F. Schaller, Physical and chemical properties of sea salt deliquescent brines as a function of temperature and relative humidity. Sci. Total Environ. 824 (2022) 154462. https://doi.org/10.1016/j.scitotenv.2022.154462

[7] J. Alcántara, D. de la Fuente, B. Chico, J. Simancas, I. Díaz, M. Morcillo, Marine atmospheric corrosion of carbon steel: A review. Materials 10 (2017) 406. https://doi.org/10.3390/ma10040406

[8] U.R. Evans, The mechanism of the so-called “dry corrosion” of metals, Trans. Faraday Soc. 19 (1923) 201-212. https://doi.org/10.1039/TF9231900201

[9] U.R. Evans, C.A.J. Taylor, Mechanism of atmospheric rusting, Corros. Sci. 12 (1972) 227-246. https://doi.org/10.1016/S0010-938X(72)90671-3

[10] S.T. Martin, Phase transitions of aqueous atmospheric particles. Chem Rev. 100 (2000) 3403-3454. https://doi.org/10.1021/cr990034t

[11] I.S. Cole, W.D. Ganther, J.D. Sinclair, D. Lau, D.A. Paterson, A study of the wetting of

metal surfaces in order to understand the processes controlling atmospheric corrosion, J. Electrochem. Soc. 151 (2004) B627. https://doi.org/10.1149/1.1809596

[12] E. Schindelholz, R.G. Kelly, Wetting phenomena and time of wetness in atmospheric corrosion: a review, Corr. Rev. 30 (2012) 135-170. https://doi.org/10.1515/corrrev-2012-0015

[13] M.S. Azevedo, C. Allély, K. Ogle, P. Volovitch, Corrosion mechanisms of Zn (Mg, Al) coated steel in accelerated tests and natural exposure: 1. The role of electrolyte composition in the nature of corrosion products and relative corrosion rate, Corros. Sci. 90 (2015) 472-481. https://doi.org/10.1016/j.corsci.2014.05.014

[14] D. Thierry, D. Persson, G. Luckeneder, K.H. Stellnberger, Atmospheric corrosion of ZnAlMg coated steel during long term atmospheric weathering at different worldwide exposure sites, Corros. Sci. 148 (2019) 338-354. https://doi.org/10.1016/j.corsci.2018.12.033

[15] M. Sakairi, S. Takagi, Effect of surface conditions and relative humidity on hydrogen permeation behavior of zinc coated steels during wet and dry corrosion, ISIJ Int. 56 (2016) 452-458. https://doi.org/10.2355/isijinternational.ISIJINT-2015-247

[16] K. Sakata, M. Sakairi, J. Kinugasa, Hydrogen Permeation Behavior of Scratch Formed on Zn Coated Steels in Simulated Atmospheric Corrosion Environment, ISIJ Int. 61(2021) 1120-1126. https://doi.org/10.2355/isijinternational.ISIJINT-2020-302

[17] C. Peng, L. Chen, M. Tang, A database for deliquescence and efflorescence relative humidities of compounds with atmospheric relevance, Fundament. Res. 2 (2022) 578-587. https://doi.org/10.1016/j.fmre.2021.11.021

[18] D.B. Blücher, J.E. Svensson, L.G. Johansson, The influence of CO2, AlCl3·6H2O, MgCl2·6H2O, Na2SO4 and NaCl on the atmospheric corrosion of aluminum. Corros. Sci. 48 (2006) 1848-1866. https://doi.org/10.1016/j.corsci.2005.05.027

[19] T. Herzog, W. Müller, W. Spiegel, J. Brell, D. Molitor, D. Schneider, Corrosion caused by dew point and deliquescent salts in the boiler and flue gas cleaning, K.J. Thomé-Kozmiensky, S. Thiel (Eds.), Waste Management, 3, Recycling and Recovery, TK Verlag, Neuruppin (2012), pp. 343-358.

[20] E. Schindelholz, B.E. Risteen, R.G. Kelly, Effect of relative humidity on corrosion of

steel under sea salt aerosol proxies: II. MgCl2, artificial seawater, J. Electrochem. Soc. 161 (2014) C460-C470. https://doi.org/10.1149/2.0231410jes

[21] X. Han, M. Sakairi, The promotion effect of aluminium ion on hydrogen entry into steel during atmospheric corrosion, Electrochim. Acta 458 (2023)142505. https://doi.org/10.1016/j.electacta.2023.142505

[22] Y. Wang, J. Yamanishi, T. Haruna, Effect of Humidity of Air on Hydrogen Absorption into Fe with Rust Layer Containing MgCl2 during Atmospheric Corrosion, ISIJ Int. 61(2021) 1143-1150. https://doi.org/10.2355/isijinternational.ISIJINT-2020-426

[23] J.R. Galvele, Transport processes and the mechanism of pitting of metals, J. Electrochem. Soc. 123 (1976) 464. https://doi.org/10.1149/1.2132857

[24] E. Akiyama, S. Li, T. Shinohara, Z. Zhang, K. Tsuzaki, Hydrogen entry into Fe and high strength steels under simulated atmospheric corrosion, Electrochim. Acta 56 (2011) 1799-1805. https://doi.org/10.1016/j.electacta.2010.09.043

[25] S. Ootsuka, S. Fujita, E. Tada, A. Nishikata, T. Tsuru, Evaluation of hydrogen absorption into steel in automobile moving environments, Corros. Sci. 98 (2015) 430-437. https://doi.org/10.1016/j.corsci.2015.05.049

[26] S. Ajito, E. Tada, A. Ooi, A. Nishikata, Hydrogen Absorption Behavior of Pre-Rusted Steels under an NaCl Droplet, J. Electrochem. Soc. 166 (2019) C243. https://doi.org/10.1149/2.0591910jes

[27] X. Han, M. Sakairi, Hydrogen permeation behavior of steel under wet/dry corrosion with changes in relative humidity at the dry period, ISIJ Int. 61 (2021) 1194-1200. https://doi.org/10.2355/isijinternational.ISIJINT-2020-555

[28] T. Prosek, D. Thierry, C. Taxén, J. Maixner, Effect of cations on corrosion of zinc and carbon steel covered with chloride deposits under atmospheric conditions, Corros. Sci. 49 (2007) 2676-2693. https://doi.org/10.1016/j.corsci.2006.11.004

[29] C. Liu, V.A. Yang, R.G. Kelly, Inhibition of Cathodic Kinetics by Zn2+ and Mg2+ on AA7050-T7451, J. Electrochem. Soc. 166 (2019) C134. http://doi.org/10.1149/2.0551906jes

[30] R.G. Pearson, Hard and soft acids and bases. J. Am. Chem. Soc. 85 (1963) 3533-3539. https://doi.org/10.1021/ja00905a001

[31] S. Zhang, T. Shibata, T. Haruna, Inhibition effect of metal cations to intergranular stress corrosion cracking of sensitized Type 304 stainless steel, Corros. Sci. 47 (2005) 1049-1061. https://doi.org/10.1016/j.corsci.2004.06.014

[32] T. Shibata, Passivity breakdown and stress corrosion cracking of stainless steel, Corros. Sci. 49 (2007) 20-30. https://doi.org/10.1016/j.corsci.2006.05.031

[33] M. Sakairi, R. Sasaki, A. Kaneko, Y. Seki, D. Nagasawa, Evaluation of metal cation effects on galvanic corrosion behavior of the A5052 aluminum alloy in low chloride ion containing solutions by electrochemical noise impedance, Electrochim. Acta, 131 (2014) 123-129. https://doi.org/10.1016/j.electacta.2014.02.010

[34] K. Otani, M. Sakairi, Effects of metal cations on corrosion of mild steel in model fresh water, Corros. Sci. 111(2016) 302-312. https://doi.org/10.1016/j.corsci.2016.05.020

[35] M. Misono, E.I. Ochiai, Y. Saito, Y. Yoneda, A new dual parameter scale for the strength of Lewis acids and bases with the evaluation of their softness, J. inorg. nucl. Chemi. 29 (1967) 2685-2691. https://doi.org/10.1016/0022-1902(67)80006-X

[36] M. Misono, Y. Saito, Evaluation of softness from the stability constants of metal-ion complexes. Bull. Chem. Soc. Jpn, 43 (1970) 3680-3684. https://doi.org/10.1246/bcsj.43.3680

[37] M.S. Islam, K. Otani, M. Sakairi, Effects of metal cations on mild steel corrosion in 10 mM Cl− aqueous solution, Corros. Sci. 131 (2018) 17-27. https://doi.org/10.1016/j.corsci.2017.11.015

[38] G. Okamoto, Passive film of 18-8 stainless steel structure and its function, Corros. Sci. 13 (1973) 471-489. https://doi.org/10.1016/0010-938X(73)90031-0

[39] M.A.V. Devanathan, Z. Stachurski, The adsorption and diffusion of electrolytic hydrogen in palladium, Proc. R. Soc. Lond. Ser. A 270 (1962) 90-102. https://doi.org/10.1098/rspa.1962.0205

[40] T. Igarashi, K. Otani, C. Kato, M. Sakairi, Y. Togashi, K. Baba, S Takagi, Hydrogen Absorption Mechanism into Iron in Aqueous Solution Including Metal Cations by Laser Ablation Tests and First-principles Calculations, ISIJ Int. 61 (2021) 1085-1090. https://doi.org/10.2355/isijinternational.ISIJINT-2020-065

[41] C.A. Schneider, W.S. Rasband, K.W. Eliceiri, NIH Image to ImageJ: 25 years of image

analysis. Nat. Methods, 9 (2012) 671-675. https://doi.org/10.1038/nmeth.2089

[42] N.C. Hosking, M.A. Ström, P.H. Shipway, C.D. Rudd, Corrosion resistance of zinc–magnesium coated steel, Corros. Sci. 49 (2007) 3669-3695. https://doi.org/10.1016/j.corsci.2007.03.032

[43] J. Winiarski, W. Tylus, K. Winiarska, I. Szczygieł, B. Szczygieł, XPS and FT-IR characterization of selected synthetic corrosion products of zinc expected in neutral environment containing chloride ions, J. Spectrosc. (Hindawi), 2018 (2018). https://doi.org/10.1155/2018/2079278

[44] P. Pedeferri (Deceased), Electrochemical Mechanism, in: L. Lazzari, L., M.P. Pedeferri (Ed.), Corrosion Science and Engineering, Engineering Materials, Springer, Cham. 2018, pp. 17-35. https://doi.org/10.1007/978-3-319-97625-9_2

[45] G. Okamoto, T. Shibata, Stability of passive stainless steel in relation to the potential of passivation treatment, Corros. Sci., 10 (1970) 371-378. https://doi.org/10.1016/S0010-938X(70)80027-0

[46] K. Gong, M. Wu, F. Xie, G. Liu, D. Sun, Effect of Cl- and rust layer on stress corrosion cracking behavior of X100 steel base metal and heat-affected zone in marine alternating wet/dry environment, Mater. Chem. Phys., 270 (2021) 124826. https://doi.org/10.1016/j.matchemphys.2021.124826

[47] H. Tamura, The role of rusts in corrosion and corrosion protection of iron and steel, Corros. Sci. 50 (2008) 1872-1883. https://doi.org/10.1016/j.corsci.2008.03.008

**Figure Captions**

Fig. 1. (a) Schematic of the electrochemical cell for the measurement of hydrogen permeation currents during corrosion. (b) Experimental setup for cyclic wet-dry corrosion tests. (c) Changes in temperature and relative humidity during one wet-dry cycle.

Fig. 2. Optical images of sample surface changes during the first cycle under (a) 10 mM NaCl, (b) 5 mM $MgCl_2$, and (c) 5 mM $ZnCl_2$.

Fig. 3. (a) Changes in hydrogen permeation current densities of the samples exposed to salt droplets during the first cycle. (b) Electric charges of the samples during each stage of the first cycle. Error bars represent standard deviation.

Fig. 4. (a)Wide-scan XPS spectra of the samples after corrosion for one and two hours in the first wet-dry cycle. (b) Narrow-scan XPS spectra of Mg 1s and Zn $2p_{2/3}$ of the samples after one hour and Zn $2p_{2/3}$ of the sample after two hours of corrosion.

Fig. 5. Optical images of surface changes in samples under deposited salts of (a) NaCl, (b) $MgCl_2$, and (c) $ZnCl_2$ during the second and third cycles of wet-cry corrosion.

Fig. 6. (a) Changes in hydrogen permeation current densities of the samples exposed to salt droplets during the last eleven cycles. (b) Electric charges of the samples in the last eleven cycles for each period of a we-dry cycle. Error bars represent standard deviation.

Fig. 7. SEM and EDS elemental mapping images of the samples after corrosion under salt droplets of (a) 10 mM NaCl, (b) 5 mM $MgCl_2$, and (c) 5 mM $ZnCl_2$ for twelve cycles.

Fig. 8. (a) SEM images of two areas marked in Fig. 7 (c) of the corroded sample under $ZnCl_2$. (b) AES spectra of the selected points in (a). (c) Comparison of the detected AES spectra in the Zn spectral range with the standard spectra.

Fig. 9. Cross-sectional images of the rust layers formed on the samples after cyclic corrosion under (a) 10 mM NaCl, (b) 5 mM $MgCl_2$, and (c) 5 mM $ZnCl_2$.

Fig. 10. Optical images and region selection for the samples after cyclic corrosion under (a) 10 mM NaCl, (b) 5 mM $MgCl_2$, and (c) 5 mM $ZnCl_2$.

Fig. 11. Hydrogen permeation charges of the samples after cyclic corrosion under five kinds of salt droplets as a function of the ratio of pitting area to exposed area.

Fig. 12. Proposed models of (a) the attack of chloride ions on the surfaces and defective sites of the passive film under aqueous NaCl solution, (b) the combination of Zn and passive film presenting a protective effect against corrosion, (c) the porous rust layer contributing to the formation of thin electrolyte layer at low humidity, and (d) the breakdown of $Zn^{2+}$-containing layer due to the increasing concentration of chloride ion as water evaporates.

**Tables**

Table 1. Summary of the preferred values of DRH and ERH of the salts at 25˚C and the parameter X of the corresponding metal cations.

| Salt | DRH (%) | ERH (%) | Reference | Cation | Parameter X [35] |
|---|---|---|---|---|---|
| NaCl | 73-77 | 41-51 | [17] | $Na^+$ | 1.01 |
| $MgCl_2·6H_2O$ | 30-35 | 9-11 | [17] | $Mg^{2+}$ | 3.54 |
| $AlCl_3·6H_2O$ | 30[a] | - | [18] | $Al^{3+}$ | 7.70 |
| $ZnCl_2$ | < 10[a] | - | [19] | $Zn^{2+}$ | 4.64 |

[a] The DRH values of $AlCl_3·6H_2O$ and $ZnCl_2$ at 25˚C are estimated from the references.

Table 2. The salt solutions used to initiate corrosion in the experiments.

| Solution | Composition | pH at 22˚C |
|---|---|---|
| 1 | 10 mM NaCl | 5.9 |
| 2 | 5 mM $MgCl_2·6H_2O$ | 5.8 |
| 3 | 3 mM $MgCl_2·6H_2O$ + 4 mM NaCl | 5.7 |
| 4 | 5 mM $ZnCl_2$ | 5.7 |
| 5 | 3 mM $ZnCl_2$ + 4 mM NaCl | 5.7 |

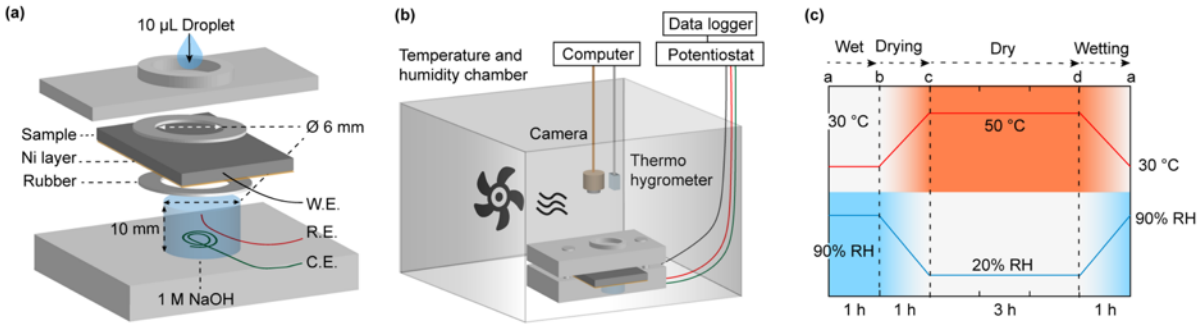


Fig. 1. (a) Schematic of the electrochemical cell for the measurement of hydrogen permeation currents during corrosion. (b) Experimental setup for cyclic wet-dry corrosion tests. (c) Changes in temperature and relative humidity during one wet-dry cycle.

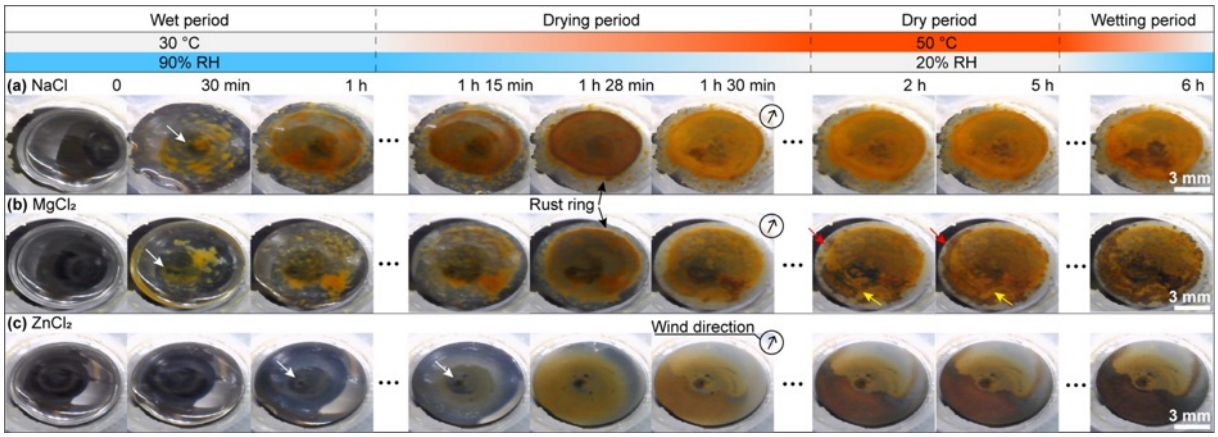


Fig. 2. Optical images of sample surface changes during the first cycle under (a) 10 mM NaCl, (b) 5 mM $MgCl_2$, and (c) 5 mM $ZnCl_2$.

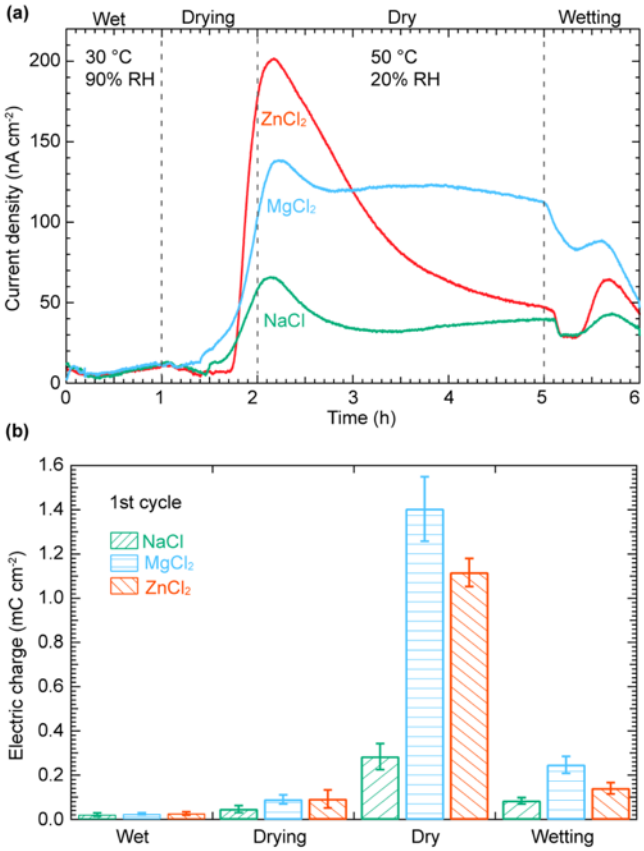


Fig. 3. (a) Changes in hydrogen permeation current densities of the samples exposed to salt droplets during the first cycle. (b) Electric charges of the samples during each stage of the first cycle. Error bars represent standard deviation.

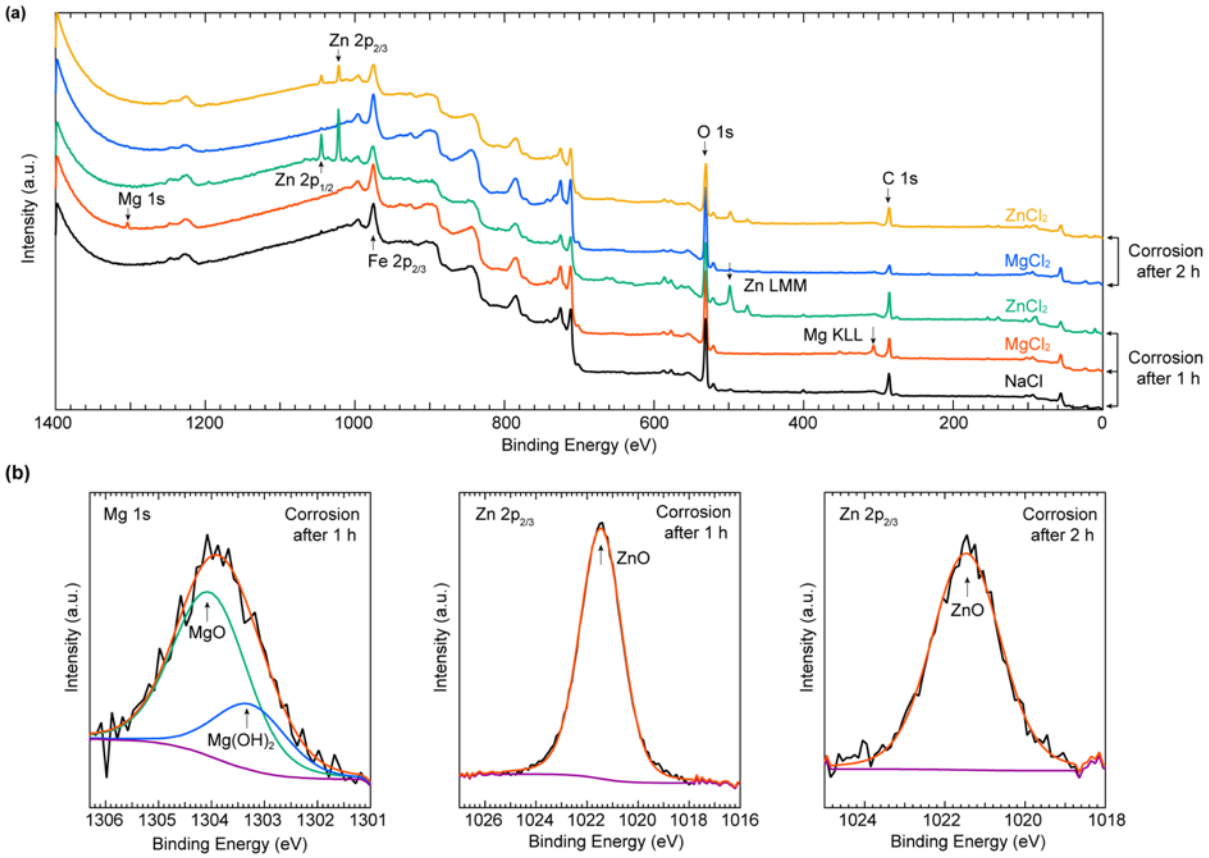


Fig. 4. (a)Wide-scan XPS spectra of the samples after corrosion for one and two hours in the first wet-dry cycle. (b) Narrow-scan XPS spectra of Mg 1s and Zn $2p_{2/3}$ of the samples after one hour and Zn $2p_{2/3}$ of the sample after two hours of corrosion.

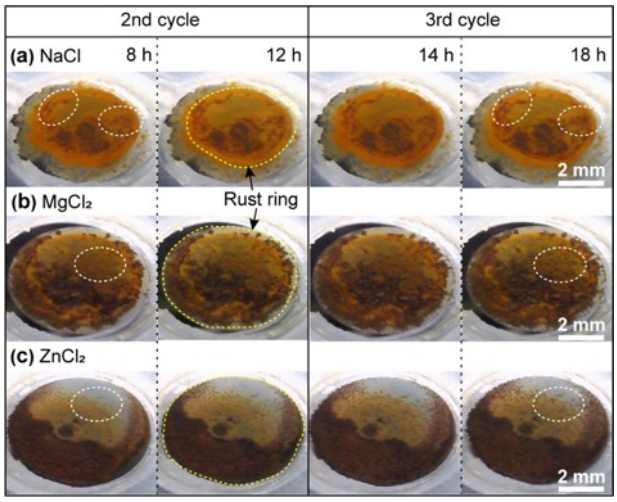


Fig. 5. Optical images of surface changes in samples under deposited salts of (a) NaCl, (b) $MgCl_2$, and (c) $ZnCl_2$ during the second and third cycles of wet-cry corrosion.

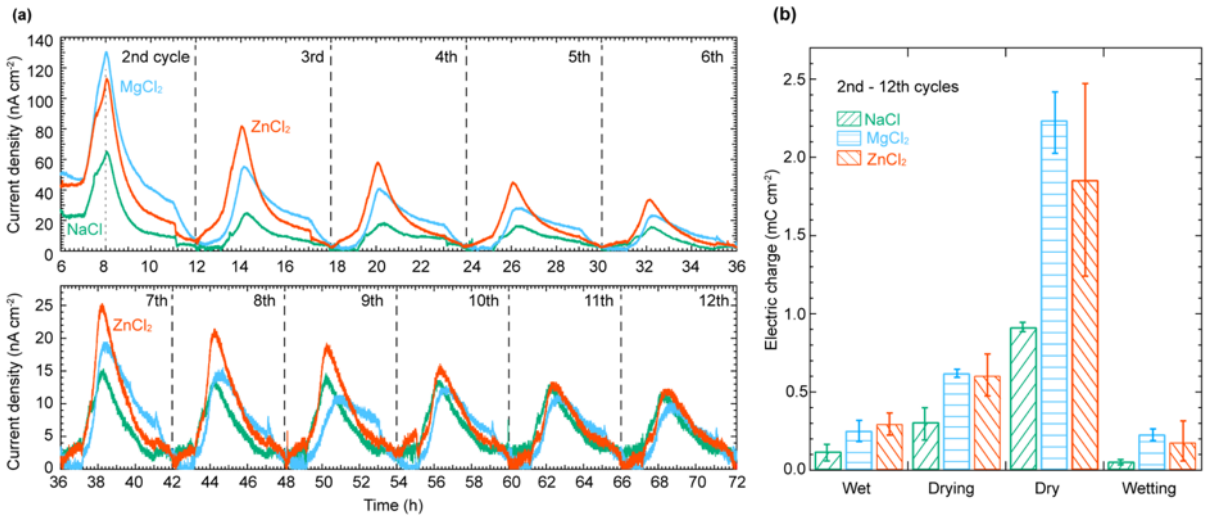


Fig. 6. (a) Changes in hydrogen permeation current densities of the samples exposed to salt droplets during the last eleven cycles. (b) Electric charges of the samples in the last eleven cycles for each period of a we-dry cycle. Error bars represent standard deviation.

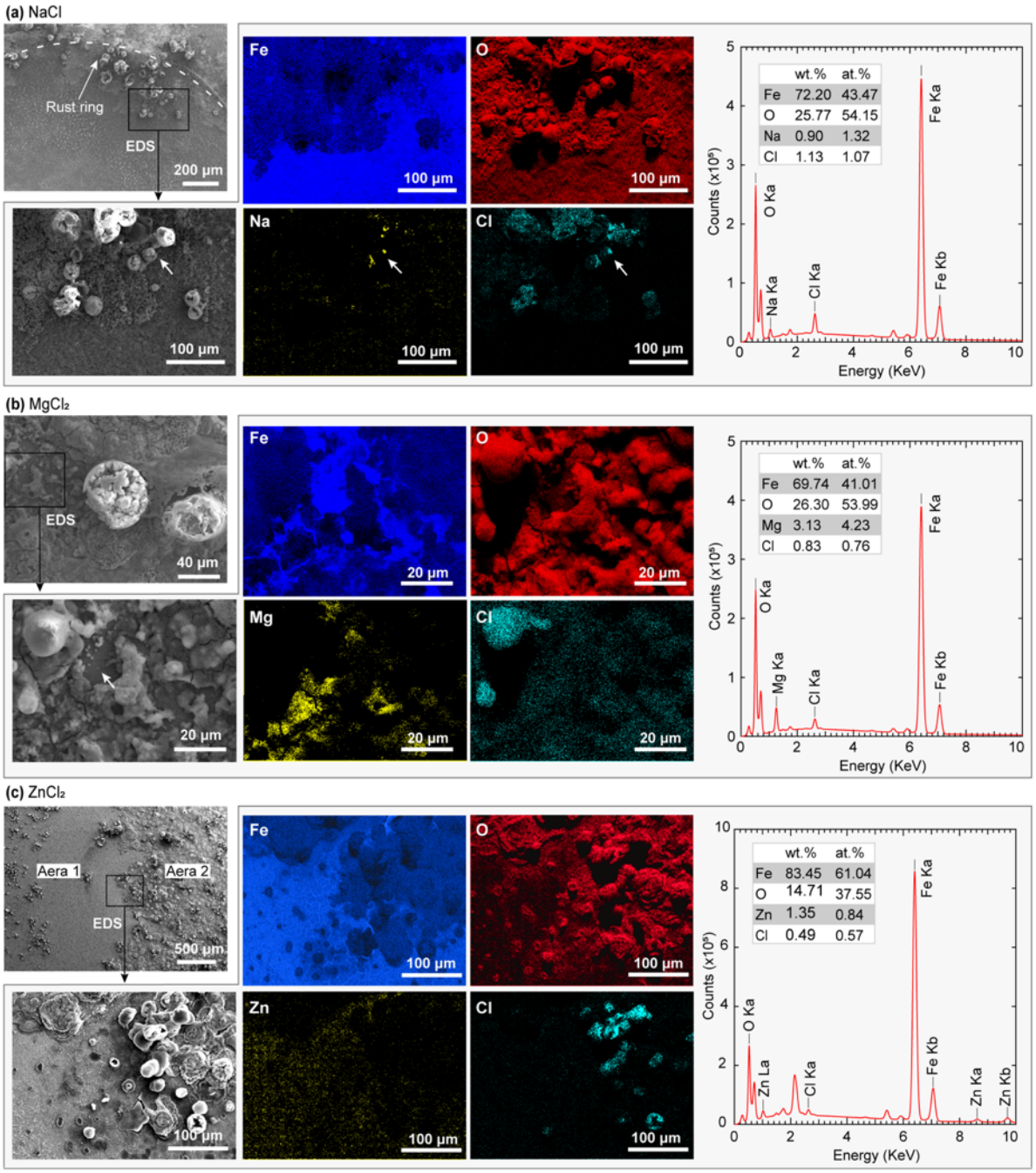


Fig. 7. SEM and EDS elemental mapping images of the samples after corrosion under salt droplets of (a) 10 mM NaCl, (b) 5 mM $MgCl_2$, and (c) 5 mM $ZnCl_2$ for twelve cycles.

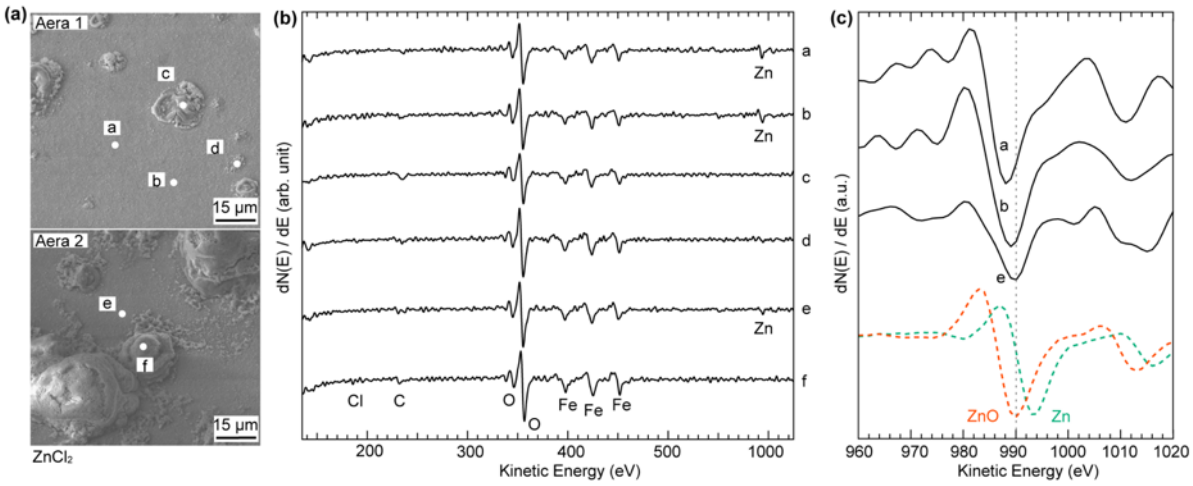


Fig. 8. (a) SEM images of two areas marked in Fig. 7 (c) of the corroded sample under $ZnCl_2$. (b) AES spectra of the selected points in (a). (c) Comparison of the detected AES spectra in the Zn spectral range with the standard spectra.

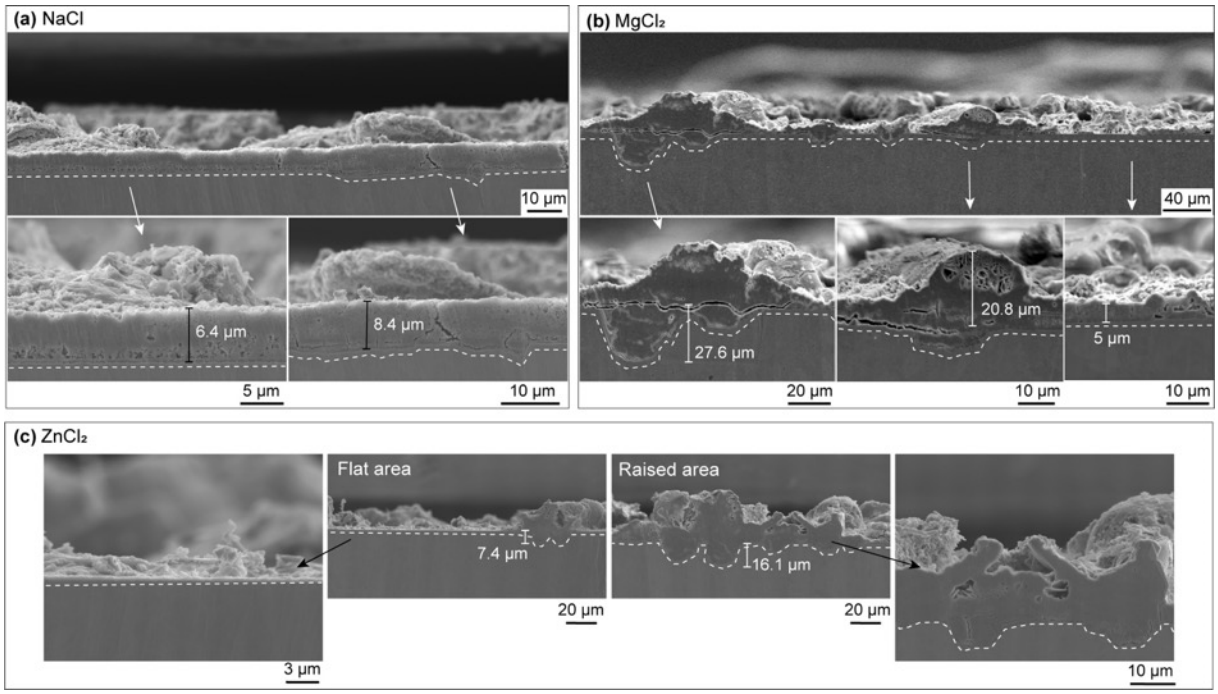


Fig. 9. Cross-sectional images of the rust layers formed on the samples after cyclic corrosion under (a) 10 mM NaCl, (b) 5 mM $MgCl_2$, and (c) 5 mM $ZnCl_2$.

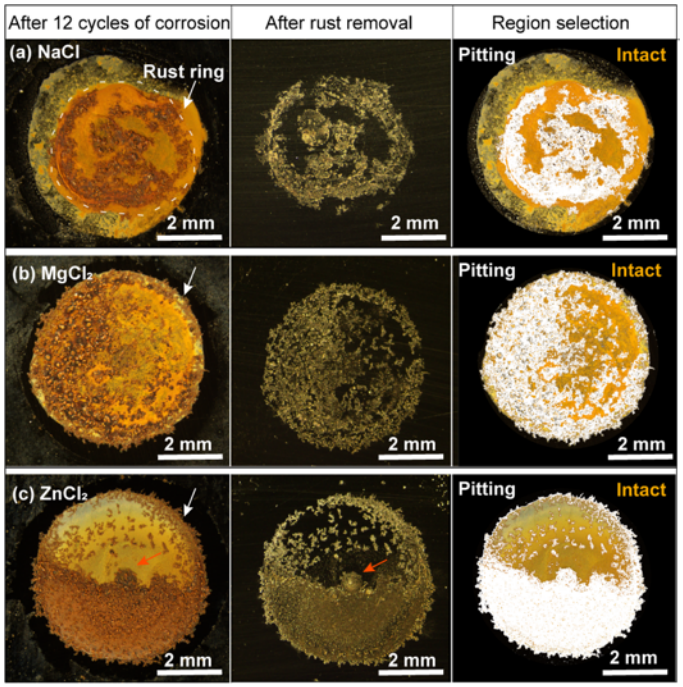


Fig. 10. Optical images and region selection for the samples after cyclic corrosion under (a) 10 mM NaCl, (b) 5 mM $MgCl_2$, and (c) 5 mM $ZnCl_2$.

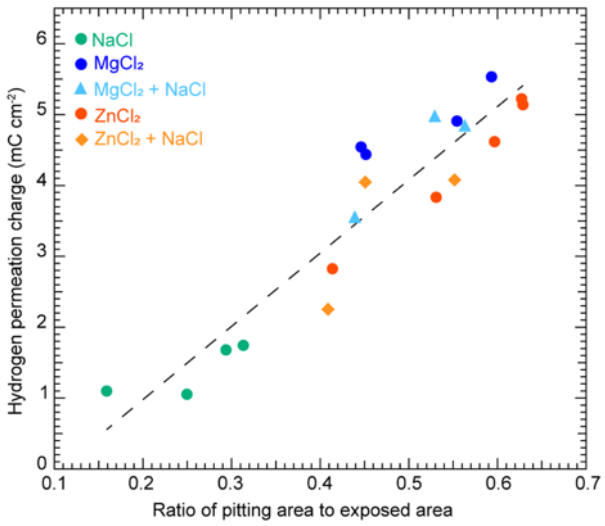


Fig. 11. Hydrogen permeation charges of the samples after cyclic corrosion under five kinds of salt droplets as a function of the ratio of pitting area to exposed area.

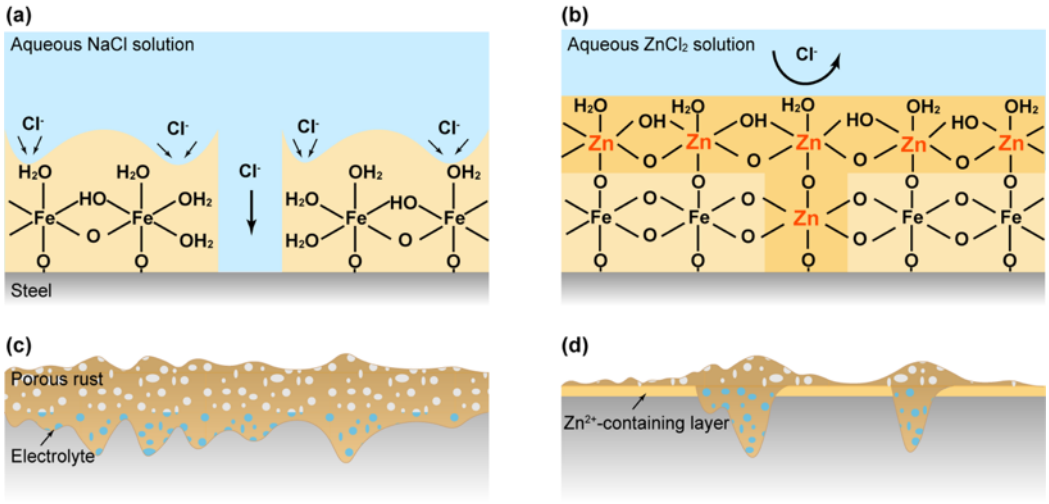


Fig. 12. Proposed models of (a) the attack of chloride ions on the surfaces and defective sites of the passive film under aqueous NaCl solution, (b) the combination of Zn and passive film presenting a protective effect against corrosion, (c) the porous rust layer contributing to the formation of thin electrolyte layer at low humidity, and (d) the breakdown of $Zn^{2+}$-containing layer due to the increasing concentration of chloride ion as water evaporates.

## Appendix A. Supplementary data

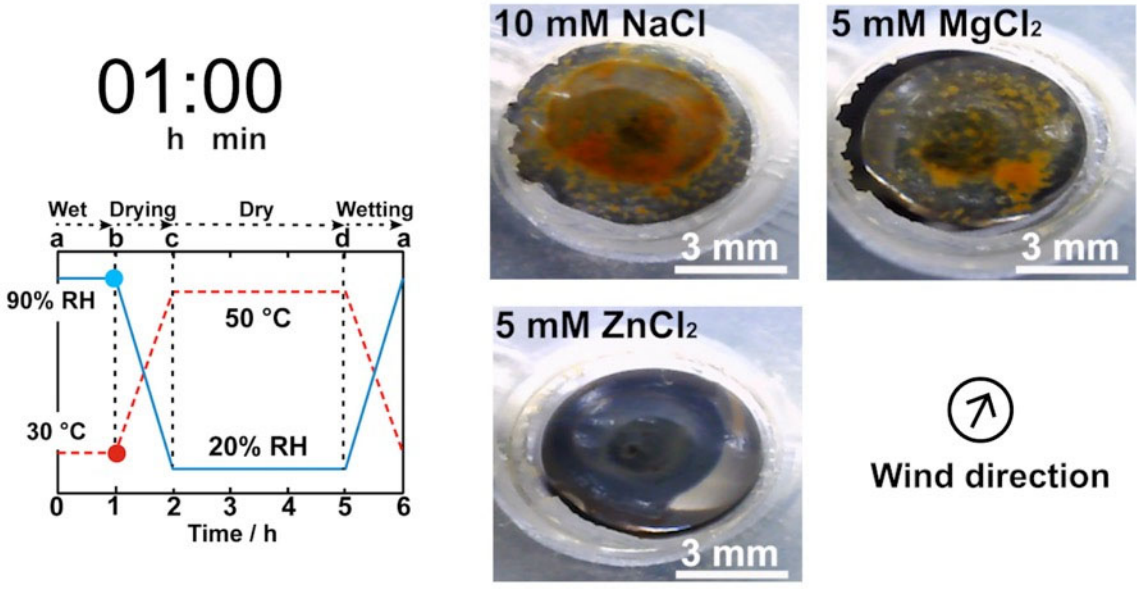


Movie S1. Time-lapse video recording of the surface changes of the samples during the initial three cycles. The video can be found online at doi:10.1016/j.corsci.2024.111993.

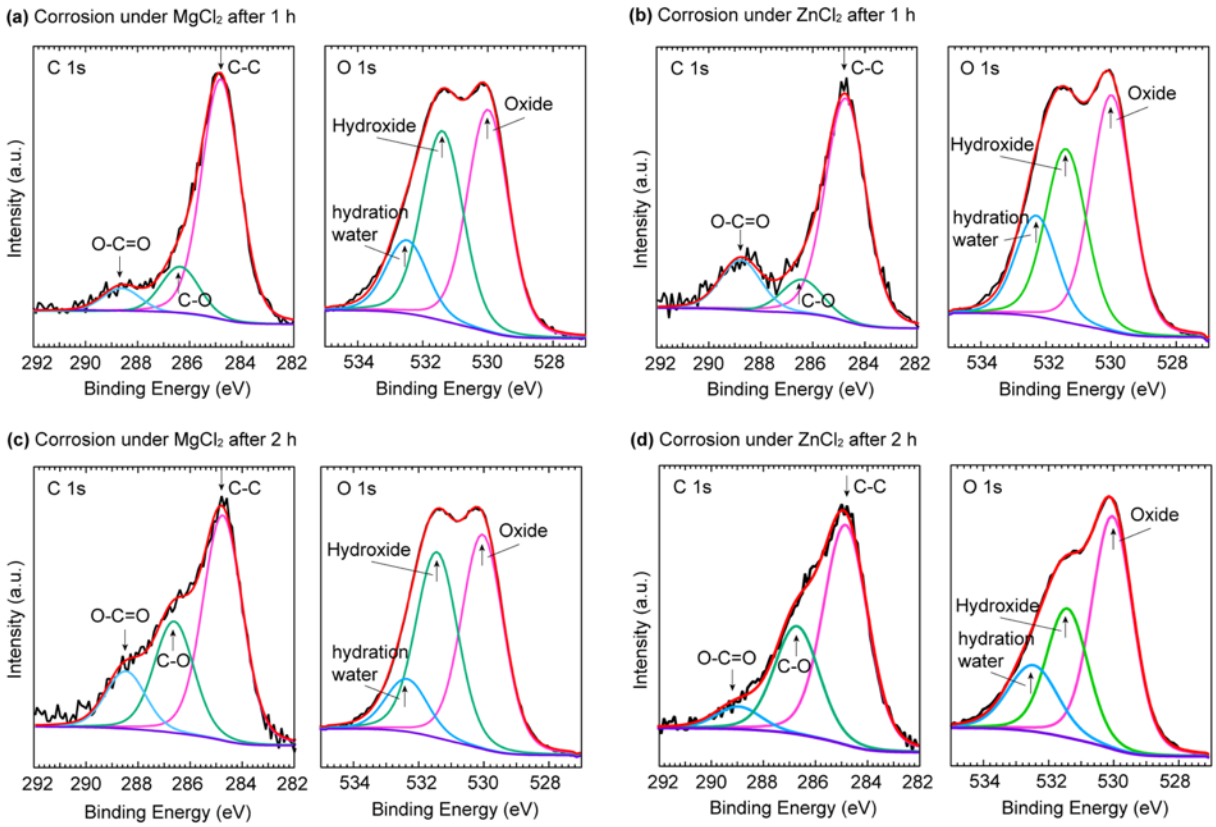


Fig. S1. Narrow-scan XPS spectra of C 1s and O 1s of the samples after the first and second hours of corrosion under 5 mM $MgCl_2$ and 5 mM $ZnCl_2$ salt droplets. The peak of 284.8 eV is related to the C-C bonds, and the peaks around 286.5 eV and 288.6 eV can be attributed to C-O and O-C=O bonds in the C 1s spectra. The peaks of 530.0 eV and 531.4 eV correspond to the oxide and hydroxide bonds, and the third peak of about 532.4 eV may be associated with hydration water in the O 1s spectra [1].

[1] NIST X-ray Photoelectron Spectroscopy Database, NIST Standard Reference Database Number 20, National Institute of Standards and Technology, Gaithersburg MD, 20899 (2000), DOI: https://dx.doi.org/10.18434/T4T88K

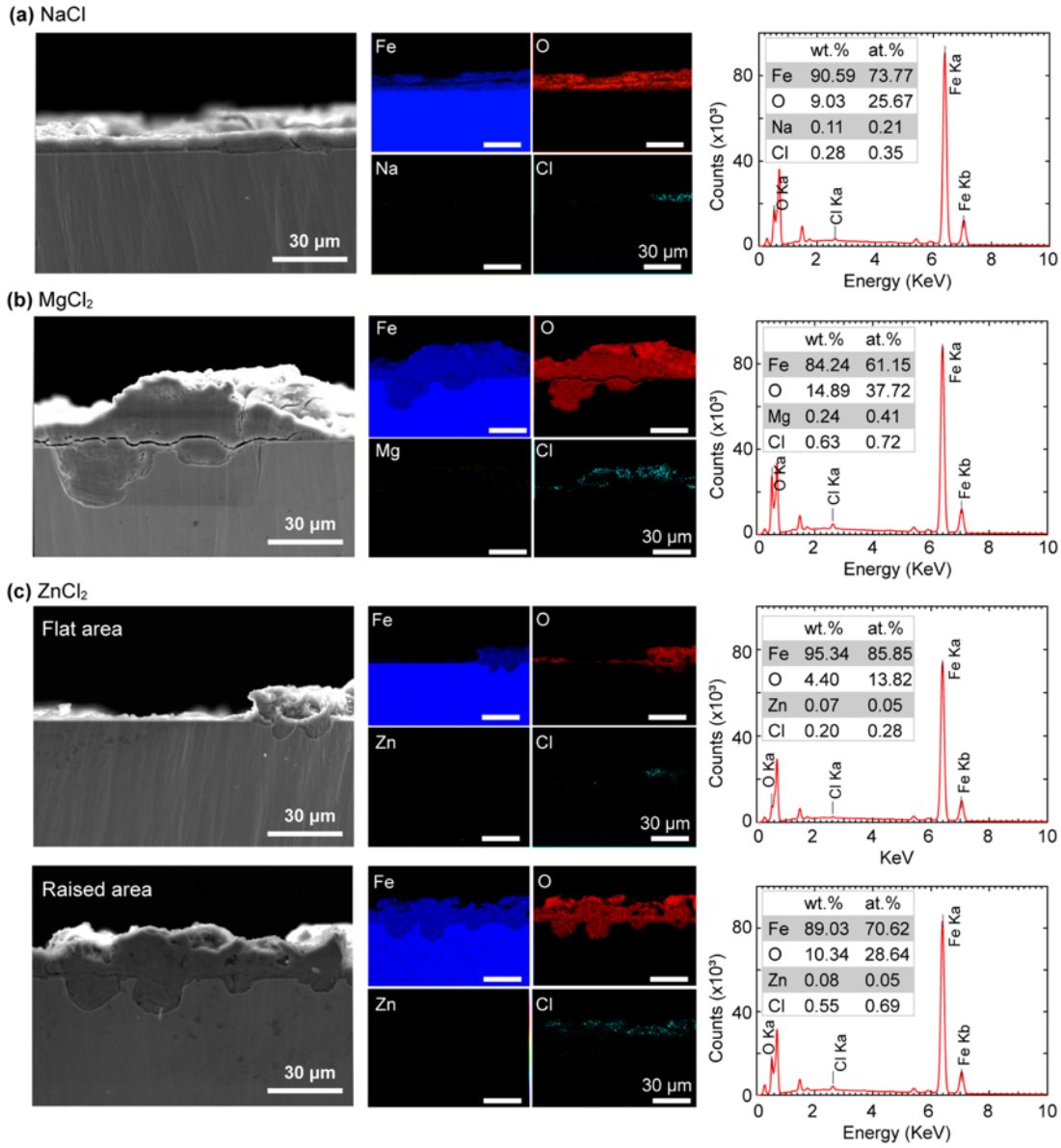


Fig. S2. EDS elemental mapping images of the cross-sectional samples after corrosion under salt droplets of (a) 10 mM NaCl, (b) 5 mM $MgCl_2$, and (c) 5 mM $ZnCl_2$ for twelve cycles.